Progress In Electromagnetics Research B, Vol. 38, 135–164, 2012

SUBCELL METHOD FOR MODELING METALLIC RESONATORS IN METAMATERIALS

L. K. Warne, W. A. Johnson, L. I. Basilio*, W. L. Langston, and M. B. Sinclair

Sandia National Laboratories, Electromagnetic Theory, P.O. Box 5800, Albuquerque, NM 87185-1152, USA

Abstract—This paper describes a subcell modeling technique for metallic resonators where the actual metal traces are replaced by a thin wire having equivalent magnetic and electric radii, as well as an impedance per unit length. The formulas for these quantities in the case of rectangular traces are given. In addition, the gap of a split-ring resonator is replaced by a lumped load. The response of the resonator can then be modeled using thin-wire algorithms in an integral equation code. It is demonstrated that the number of unknowns and runtime can be reduced by factors of a thousand using the subcell models. This is particularly important in cases where metamaterial designs with tapered properties are encountered and periodic boundary conditions are not applicable, because with this simplification larger numbers of resonator cells can be handled.

1. INTRODUCTION

Metamaterials (MMs) are artificially-structured materials often made up of resonant metallic structures in each of the cells [1]. Since applications of these materials usually require gradients of properties and ultimately introduce boundary effects, and because the behavior of the resonant structures can be more sensitive to the properties of neighboring cells and boundaries, periodic-modeling assumptions often cannot be used. Thus, there is great interest in reducing the size of the computation in each cell so that collections of cells can be directly modeled. However it is often found that the metallic-loss properties, which determine the effective absorption of the metamaterial, must be accurately modeled and this can be a challenge due to the extra scales

Received 11 November 2011, Accepted 5 January 2012, Scheduled 13 January 2012

* Corresponding author: Lorena I. Basilio (libasil@sandia.gov).

of length introduced by the conductive materials (particularly as the frequency increases). Because these metallic structures often involve narrow traces, there is an opportunity to reduce the complexity of the problem, while simultaneously improving modeling accuracy. This can be done by embedding known descriptions of the trace properties into the simulation tools, thus forming subcell descriptions of the metallic elements making up the resonator structures. (The use of single facets across the width of a thin strip [2] is a very simple and familiar example of such an unknown reduction approach and can work if all the conductive scales of length are large compared to the cross sectional dimensions). This approach allows the resonant distributions of current to still respond to neighbor proximity effects, but removes the burden of tracking these other electrical length scales in the simulation.

This paper discusses these subcell descriptions of narrow metallic-trace elements, which have recently been presented [3], and provides simple formulas for estimating them (these apply to geometries where the trace lengths are considerably larger than the cross sections). These subcell descriptions include the per unit length capacitive, inductive, and absorptive properties of metallic traces on substrates, as well as lumped loads at gaps in the structures (which are used to provide reactances to downshift the resonances in frequency). Subcell models for both microwave and infrared-frequency regions are addressed. Examples are given illustrating the approach with both electric and magnetic resonator structures, which form the essential components required for negative index metamaterials. Split-ring resonators (SRRs), as shown in Figure 1(a), are frequently used for

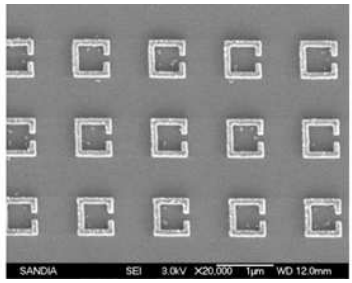

(a) (b)

Figure 1. (a) Thin metallic traces of split ring resonators (SRRs) which generate a magnetic dipole moment orthogonal to the loop (there is also an in-plane electric moment). The gap can be designed to downshift the resonance. (b) A loaded electric dipole resonator can generate the required electric dipole moment.

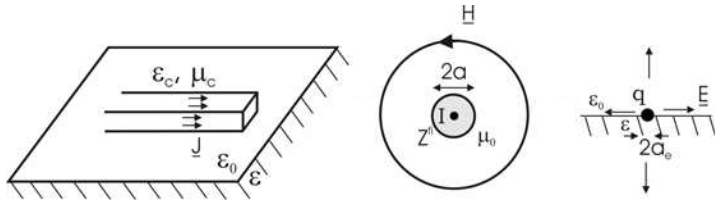

(a) (b) (c)

Figure 2. (a) A metallic trace carrying current density J with internal electric and magnetic properties ε_c and μ_c, on a substrate with permittivity ε. (b) The equivalent wire of radius a for the external inductance and internal impedance per unit length. (c) The equivalent wire of radius a_e embedded in the substrate interface for the capacitance per unit length.

the magnetic components, whereas various types of dipoles are often encountered for the electric component. An example of a loaded dipole is shown in Figure 1(b), where in the infrared, polaritonic materials with intrinsic negative permittivities can be used as the load to downshift the resonance. With subcell descriptions of these types of resonators one thousand to one reductions in computational complexity can be achieved, thereby enabling accurate simulations of complex metamaterial applications including lenses, prisms, and cloaks.

2. RECTANGULAR TRACES AND THIN WIRES

The idea behind the metallic trace simplification is to replace the actual metallic traces of width w and thickness t such as shown in Figure 2(a) (which form the resonant structure) with thin wires having the same electrical properties, such as shown in Figures 2(b) and 2(c), but requiring only total current unknowns along the trace to be tracked. The external inductance per unit length leads to an equivalent radius a for the wire; this radius together with an internal impedance per unit length Z^{fi} associated with the finite conductivity of the wire replaces the trace in a homogeneous medium. If the trace is placed near (resting on or embedded in) a dielectric substrate, then the capacitance per unit length in general leads to a different electric equivalent radius a_e for a wire embedded in the interface.

2.1. Magnetic Equivalent Radius

The (magnetic) equivalent radius of a rectangular conductor is [4, 5]

$$a = C_1 / \left(2\kappa^2\right) \tag{1}$$

where κ is found from the transcendental equation

$$\frac{t}{w} = \frac{E(\kappa) - \kappa'^2 K(\kappa)}{E(\kappa') - \kappa^2 K(\kappa')} \tag{2}$$

$$\kappa' = \sqrt{1-\kappa^2} \tag{3}$$

and C_1 is found from either of

$$\frac{w}{2C_1}\kappa^2 = E(\kappa') - \kappa^2 K(\kappa') \tag{4}$$

or

$$\frac{t}{2C_1}\kappa^2 = E(\kappa) - \kappa'^2 K(\kappa) \tag{5}$$

where the complete elliptic integrals are [6]

$$E(\kappa) = \int_0^{\pi/2} \sqrt{1-\kappa^2 \sin^2\theta}\, d\theta \tag{6}$$

$$K(\kappa) = \int_0^{\pi/2} d\theta / \sqrt{1-\kappa^2 \sin^2\theta}\, d\theta \tag{7}$$

While the above formulas define the equivalent radius, a simple and accurate fit to the magnetic equivalent radius is given by

$$a/(w/4) \approx 1 + \frac{t}{\pi w}\left\{c_1 \ln(w/t) - \pi + \Gamma^2(1/4)/\sqrt{\pi}\right\} \tag{8}$$

for $t \leq w$ where $c_1 = 3/4$ and the gamma function $\Gamma(1/4) = 3.6256099$. Conveniently, t and w are interchanged for the case of $t > w$. Figure 3 shows a comparison of the numerical solution of the preceding equations versus the simple fit (8) for the equivalent magnetic wire radius (the remaining three comparisons of other conformal mapping parameters with simple fits in this figure will be discussed in Section 2.3).

2.2. Electric Equivalent Radius on Substrate

A formula for the electric equivalent radius is concocted by a simple parallel-series decomposition argument and the known limiting cases for the result. We want the local (out to distance $\rho_0 \gg a,\ a_e$) capacitance per unit length to have the form of a parallel combination (above and below the interface)

$$C_{\rho_0} \sim \frac{\pi(\varepsilon_0 + \varepsilon)}{\ln(\rho_0/a_e)} \tag{9}$$

where the equivalent cylinder is half embedded in the interface (half above and half below) and the fields from the cylinder to infinity are

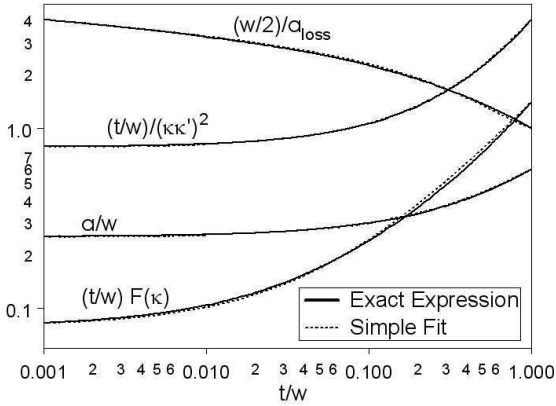

Figure 3. Comparing the numerical solutions of the conformal-mapping expressions to the simple fit formula values. Comparisons for the equivalent magnetic wire radius, the inverse loss radius, the third term function, and the square of the inverse product $\kappa\kappa'$ are included.

purely radial and $\varepsilon_0 \approx 8.854188\,\mathrm{pF/m}$ is the electric permittivity of free space. We try the series decomposition (where the capacitance outside of distance a_1 is the same parallel combination, approximating the fields outside this radius as radial fields only),

$$1/C_{\rho_0} \approx \frac{\ln(\rho_0/a_1)}{\pi(\varepsilon+\varepsilon_0)} + 1/C_{a_1} \tag{10}$$

where the capacitance inside the radius a_1 is taken as

$$C_{a_1} = \frac{2\pi\varepsilon_0}{\ln(a_1/a)} + \frac{\pi(\varepsilon-\varepsilon_0)}{\ln(a_1/a_0)} \tag{11}$$

and the thin strip limit is denoted as

$$a_0 = w/4 \tag{12}$$

This construction of C_{a_1} is chosen because we want a_e to go to the magnetic equivalent radius a when the interface is not present $\varepsilon = \varepsilon_0$ and to go to the strip result a_0 when the substrate capacitance is dominant $\varepsilon \gg \varepsilon_0$. Equating this approximate form (10) with (9) gives

$$\ln\left(\frac{a_e}{a_0}\right) / \ln\left(\frac{a}{a_0}\right) \approx \frac{2\ln(a_1/a_0)}{(1+\varepsilon/\varepsilon_0)\ln(a_1/a) + 2\ln(a/a_0)} \tag{13}$$

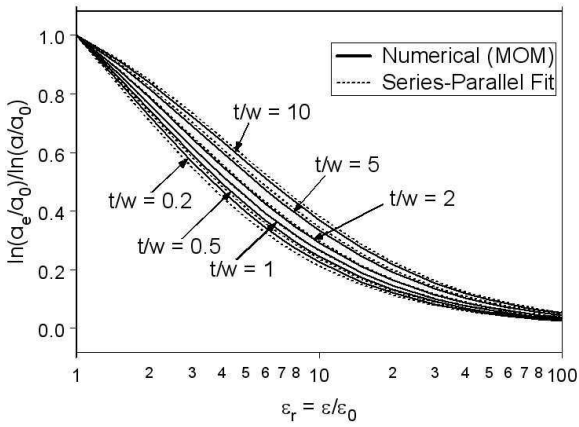

Figure 4. Comparison of the numerical solution for the electric equivalent radius and results from simple parallel-series fit formula. Several cross-section dimensions for the metallic trace are considered.

Note that both limits of $\varepsilon/\varepsilon_0$ hold without yet choosing a_1. A reasonable choice for a_1 is

$$a_1 = 4a \tag{14}$$

(in the case of a thin structure a_1 represents the total width of the strip, in the case of a square cross-section it represents 2.36 times the width or 1.67 times the diagonal). The results from this simple fit are shown in Figure 4 along with the numerical solution described in Section 2.2.1. Excellent agreement is obtained over a wide range of permittivities and aspect ratios.

2.2.1. Numerical Solution

The two-dimensional numerical solution shown in Figure 4 is now given. The scalar potential with piecewise-constant surface charge densities σ_n on the two-dimensional conductor and image charges in the dielectric half space (here we specialize to a rectangle of width w and thickness t) is

$$-2\pi\varepsilon_0\phi = \sum_{n=1}^{N} \sigma_n \int_{x_n-\Delta_n/2}^{x_n+\Delta_n/2} \ln\sqrt{(x-x')^2+(y-y_n)^2}\,dx' + \sum_{n=N+1}^{M+N} \sigma_n \int_{y_n-\Delta_n/2}^{y_n+\Delta_n/2} \ln\sqrt{(x-x_n)^2+(y-y')^2}\,dy'$$

$$+\frac{\varepsilon_0-\varepsilon}{\varepsilon_0+\varepsilon}\sum_{n=1}^{N}\sigma_n\int_{x_n-\Delta_n/2}^{x_n+\Delta_n/2}\ln\sqrt{(x-x')^2+(y+y_n)^2}dx'$$
$$+\frac{\varepsilon_0-\varepsilon}{\varepsilon_0+\varepsilon}\sum_{n=N+1}^{M+N}\sigma_n\int_{y_n-\Delta_n/2}^{y_n+\Delta_n/2}\ln\sqrt{(x-x_n)^2+(y+y')^2}dy' \quad (15)$$

where

$$\int\ln\sqrt{(x'-x)^2+c^2}dx' = (x'-x)\left\{\ln\sqrt{(x'-x)^2+c^2}-1\right\} + c\arctan\left(\frac{x'-x}{c}\right) \quad (16)$$

Now on the surface we set

$$\phi(x_m,y_m)=V_0,\quad m=1,\ldots,M+N \quad (17)$$

At a large distance $\sqrt{x^2+y^2}=\rho\to\rho_0$ we see from this representation that

$$\phi(\rho_0)\sim -q\frac{\ln(\rho_0)}{\pi(\varepsilon+\varepsilon_0)} \quad (18)$$

where the total charge per unit length is

$$q=\sum_{n=1}^{N+M}\sigma_n\Delta_n \quad (19)$$

The difference potential is given by

$$V=\phi(w/2)-\phi(\rho_0)=V_0+q\frac{\ln(\rho_0)}{\pi(\varepsilon+\varepsilon_0)}=q/C_{\rho_0}=q\frac{\ln(\rho_0/a_e)}{\pi(\varepsilon+\varepsilon_0)} \quad (20)$$

where a_e is the equivalent radius or

$$-\ln a_e=\pi(\varepsilon+\varepsilon_0)V_0/q \quad (21)$$

We find that for a metallic design with $w=0.12\,\mu\text{m}$, $t=0.1\,\mu\text{m}$ (corresponding to an aspect ratio $t/w=5/6$), and half space $\varepsilon/\varepsilon_0\approx 10.8924$, the electric equivalent radius is $a_e=0.036\,\mu\text{m}$. This design is one that will be repeatedly considered throughout the paper and is referred to as 'design B'.

2.3. Impedance Per Unit Length

The impedance per unit length of rectangular conductors is now summarized. Expressions for various limits of the conductor dimensions to the electrical length scales associated with the losses

are given. These length scales are the penetration depth (or skin depth, which is of the order of the inverse of the imaginary part of the propagation constant in the metal) and the ratio of the surface impedance Z_s to $\omega\mu_0$. By comparing these results to numerical solutions, it is illustrated that the concatenation of these expressions gives reasonable values for the impedance per unit length over the entire range of these parameters.

The impedance per unit length of an isolated infinitely long conductor is not defined. However, we can define the impedance per unit length by including only the magnetic flux around the long conductor out to a finite but large radius ($\rho_0 \gg a$). Then we can write this as [7] (time dependence $e^{-i\omega t}$ is suppressed throughout)

$$Z_{\rho_0} \sim Z^{fi} - i\omega L^{pe}_{\rho_0} \tag{22}$$

where the external (perfectly conducting) inductance per unit length is

$$L^{pe}_{\rho_0} \sim \frac{\mu_0}{2\pi} \ln(\rho_0/a) \tag{23}$$

The remaining quantity Z^{fi} is the internal impedance due to the finite conductivity of the metal (it includes magnetic field perturbations on the outside due to the finite conductivity); this is the quantity of interest to distribute along thin-wire models to account for the internal impedance of the actual conductors.

2.3.1. Metal Resonator Properties

Some loss parameters of the metals are now summarized first in the microwave frequency regime and then in the infrared. In particular, the surface impedances calculated here are later used for determining the per unit-length impedances for the wire models in the two frequency regimes.

Microwave A microwave example is aluminum with a conductivity of $\sigma \approx 3.7 \times 10^7\,\mathrm{S/m}$ [8]. In the microwave region the internal propagation constant is

$$\gamma = (1+i)/\delta \tag{24}$$

where the skin depth is

$$\delta = \sqrt{2/(\omega\mu\sigma)} \tag{25}$$

and the magnetic permeability for aluminum (and gold for the infrared example considered next) is that of free space $\mu = \mu_0 = 4\pi \times 10^{-7}\,\mathrm{H/m}$. The surface impedance of a conductive half space is

$$Z_s = \frac{\omega\mu}{\gamma} = (1-i)R_s \tag{26}$$

where

$$R_s = 1/(\sigma\delta) \tag{27}$$

Note that the impedance scale of length is of order

$$2R_s/(\omega\mu_0) = \nu\delta \tag{28}$$

where the ratio of the internal to external magnetic permeabilities is denoted by

$$\nu = \mu/\mu_0 \tag{29}$$

Infrared The electric permittivity for gold in the infrared at a ten-micron wavelength from the Sandia National Laboratories microfab data is

$$\varepsilon/\varepsilon_0 = -4100 + i1400 \tag{30}$$

yielding a propagation constant of

$$\begin{aligned}\gamma &= k\sqrt{\varepsilon_r} = k\sqrt{4332.436e^{-i0.329+i\pi}} = 41.357\,\mu\text{m}^{-1}ie^{-i0.1645} \\ &= (6.77 + i40.8)\,\mu\text{m}^{-1}\end{aligned} \tag{31}$$

Here the free-space wavenumber is

$$k = \omega\sqrt{\mu_0\varepsilon_0} \tag{32}$$

The surface impedance of a half space is

$$Z_s = \frac{\omega\mu}{\gamma} = \sqrt{\mu_0/\varepsilon} = \frac{k\sqrt{\mu_0/\varepsilon_0}}{(6.77 + i40.8)\,\mu\text{m}^{-1}} = (0.94 - i5.65)\,\text{Ohms} \tag{33}$$

Note that the impedance scale of length is of order $Z_s/(\omega\mu_0)$, which is the same as the inverse propagation constant in the metal times the ratio of the internal to external magnetic permeabilities ν (which is typically near unity in this frequency range).

2.3.2. High-frequency Rectangle

In this case we assume the rectangular cross-section dimensions are much larger than the penetration depth. For a rectangular conductor with dimensions $w = 2b$ and $t = 2c$ we find [7]

$$\begin{aligned}Z^{fi} \sim \frac{Z_s}{2\pi a_{\text{loss}}} + 4(A_0/I)^2 C_E + \left(\frac{Z_s}{2\pi a}\right)\Bigg[\left(\frac{1}{2a}\right)\left(\frac{Z_s}{-i\omega\mu_0}\right)F(\kappa) \\ +O\left(\left(\frac{1}{\gamma a}\right)^{4/3}, \left(\frac{Z_s}{-i\omega\mu_0 a}\right)^{4/3}\right)\Bigg]\end{aligned} \tag{34}$$

where the first term results from integration of the square of the perfectly conducting magnetic field (determined from conformal

mapping) around the perimeter of the rectangle [9], where it is convenient to defines $a_{\rm loss}$ by means of

$$K(\kappa) + K\left(\kappa'\right) = \pi a/a_{\rm loss} \tag{35}$$

The third term in (34) uses [7]

$$\begin{aligned}\left(\pi\kappa\kappa'\right)^2 F(\kappa) \;=\; & E(\kappa)\left\{E(\kappa) - E\left(\kappa'\right) + K\left(\kappa'\right)\right\} \\ & +\kappa'^2\left\{E\left(\kappa'\right)K(\kappa) - 2E(\kappa)K(\kappa)\right. \\ & \left.+K(\kappa)K(\kappa) - E(\kappa)K\left(\kappa'\right)\right\} \\ & +E\left(\kappa'\right)\left\{E\left(\kappa'\right) - E(\kappa) + K(\kappa)\right\} \\ & +\kappa^2\left\{E(\kappa)K\left(\kappa'\right) - 2E\left(\kappa'\right)K\left(\kappa'\right)\right. \\ & \left.+K\left(\kappa'\right)K\left(\kappa'\right) - E\left(\kappa'\right)K(\kappa)\right\}\end{aligned} \tag{36}$$

and the second term results from losses at the four corners of the rectangle, with local field $H_\rho \sim A_0/\rho^{1/3}$, $\rho \to 0$

$$A_0/I = \frac{\kappa}{2\pi\left(3\kappa' C_1^2\right)^{1/3}} = \frac{1}{2\pi\left(12\kappa'\kappa a^2\right)^{1/3}} \tag{37}$$

with

$$C_E = -i\omega\mu\left(\frac{i}{\gamma}\right)^{4/3}\frac{2^{5/3}}{\sqrt{3}}D_c(\nu) = Z_s\left(\frac{i}{\gamma}\right)^{1/3}\frac{2^{5/3}}{\sqrt{3}}D_c(\nu) \tag{38}$$

In addition, the parameters $D_c(\nu)$, A_c, D_0, D_∞, and D_1 are given by

$$D_c(\nu) \approx \frac{A_c D_0 + D_\infty \nu^{15/12}}{A_c + \nu^{11/12}} \tag{39}$$

$$A_c = \frac{D_1 - D_\infty}{D_0 - D_1} \tag{40}$$

$$D_0 = D_c(0) = \frac{\Gamma(1/3)}{2^{1/3}}\left[1 - 3\left\{\Gamma(2/3)/\Gamma(1/3)\right\}^3\right] \approx 1.30247 \tag{41}$$

$$D_\infty = \lim_{\nu\to\infty}\left[D_c(\nu)/\nu^{1/3}\right] = -\frac{3\pi^2 2^{1/3}}{4\Gamma^2(1/3)} \approx -1.29951 \tag{42}$$

and

$$D_1 = D_c(1) \approx -0.360 \tag{43}$$

The limit of a square cross-section ($w = t$) with $\kappa = \kappa' = 1/\sqrt{2}$, $a = w\Gamma^2(1/4)/(4\pi^{3/2}) \approx 1.180341b$, $(A_0/I)^3 = 1/[3w^2\Gamma^4(1/4)]$ gives

$$\begin{aligned}Z^{fi} \sim \left(\frac{Z_s}{\pi w}\right)\left[1 + \left(\frac{i2}{\gamma a}\right)^{1/3}\left(\frac{w}{2\pi a}\right)\frac{2^{5/3}}{3^{7/6}}D_c(\nu) + \left(\frac{1}{w}\right)\left(\frac{Z_s}{-i\omega\mu_0}\right)\right. \\ \left. +O\left(\left(\frac{1}{\gamma w}\right)^{4/3}, \left(\frac{Z_s}{-i\omega\mu_0 w}\right)^{4/3}\right)\right]\end{aligned} \tag{44}$$

and for $\nu = \mu/\mu_0 = 1$ (recall that $w = 2b$)

$$Z^{fi} \sim \frac{Z_s}{2\pi b}\left[1 + (-0.102)\left(\frac{i}{\gamma b}\right)^{1/3} + \left(\frac{1}{2b}\right)\left(\frac{Z_s}{-i\omega\mu_0}\right) + O\left(\left(\frac{1}{\gamma b}\right)^{4/3}, \left(\frac{Z_s}{-i\omega\mu_0 b}\right)^{4/3}\right)\right] \tag{45}$$

Conformal Mapping Parameter Fits In this section, approximate expressions for the calculation of Z^{fi} are introduced as potential alternatives for simplifying the wire-model analysis. The first term of the impedance per unit length (34) can be found using the approximate expression

$$(w/2)/a_{\text{loss}} \approx 1 + \frac{1}{\pi}(1 - t/w)\ln(4\pi w/t) - \frac{t}{\pi^2 w}\left[\ln(4\pi w/t) + \pi/2\right]\ln(w/t) \tag{46}$$

while the third term in (34) can be found using the approximate expression

$$(t/w)F(\kappa) \sim \frac{1}{4\pi} + \frac{t}{4\pi^2 w}\left\{\ln(16w/t)\ln(w/t) - \pi + \frac{\Gamma^4(1/4)}{\pi}\right\} \tag{47}$$

Furthermore, the second term of the impedance per unit length involves the product $\kappa\kappa'$, the inverse square of which is fit by

$$(t/w)/\left(\kappa\kappa'\right)^2 \approx \frac{\pi}{4}\left[1 + \frac{t}{\pi w}\left\{\ln(w/t) - \pi + \frac{16}{1 + 4/\pi}\right\}\right]\left(1 + \frac{4t}{\pi w}\right) \tag{48}$$

A comparison between the numerical solutions and these simple fits for the inverse loss radius, the third term function, and the square of the inverse product $\kappa\kappa'$ (needed in the second term for field strength) are included in Figure 3. Excellent agreement is observed for t/w values ranging from a thin strip to a square-cross section trace.

2.3.3. Low-frequency Rectangle

Next we suppose that the penetration depth is large compared to the cross-sectional dimensions of the rectangle. Assuming a rectangular cross section of area $A = wt = (2b)(2c)$ then in the microwave case

$$Z^{fi} \sim R^{fi} - i\omega L^{fi} \tag{49}$$

where

$$R^{fi} = 1/(A\sigma) \tag{50}$$

and the general rectangular conductor with internal magnetic permeability equal to the external magnetic permeability $\mu = \mu_0$ has the total (including internal and external contributions) local (including magnetic flux out to a large distance ρ_0) inductance per unit length L_{ρ_0} [7] of

$$\begin{aligned} & L_{\rho_0} - \frac{\mu_0}{2\pi}\ln(\rho_0) \\ & \sim -\frac{\mu_0}{2\pi}\left[\begin{array}{l} \ln(\sqrt{bc})+\ln(2)-\frac{25}{12}+\frac{2}{3}\left\{\frac{b}{c}\arctan\left(\frac{c}{b}\right)+\frac{c}{b}\arctan\left(\frac{b}{c}\right)\right\} \\ +\frac{1}{4}\left\{\left(1-\frac{b^2}{3c^2}\right)\ln\left(1+\frac{c^2}{b^2}\right)+\left(1-\frac{c^2}{3b^2}\right)\ln\left(1+\frac{b^2}{c^2}\right)\right\} \end{array}\right] \end{aligned} \tag{51}$$

The internal inductance per unit length can be defined as

$$L^{fi} = L_{\rho_0} - L^{pe}_{\rho_0} \tag{52}$$

where in the square limit ($c = b$) this internal inductance becomes

$$\begin{aligned} L^{fi} &= \frac{\mu_0}{2\pi}\left[\ln(a/b) + \frac{25}{12} - \frac{4}{3}\ln(2) - \frac{\pi}{3}\right] \\ &= \frac{\mu_0}{2\pi}\left[\ln\left\{\Gamma^2\left(\frac{1}{4}\right)/\left(2\pi^{3/2}\right)\right\} + \frac{25}{12} - \frac{4}{3}\ln(2) - \frac{\pi}{3}\right] \qquad (53) \\ &\approx \frac{\mu_0}{2\pi}\ln(1.3201463233) \qquad (54) \end{aligned}$$

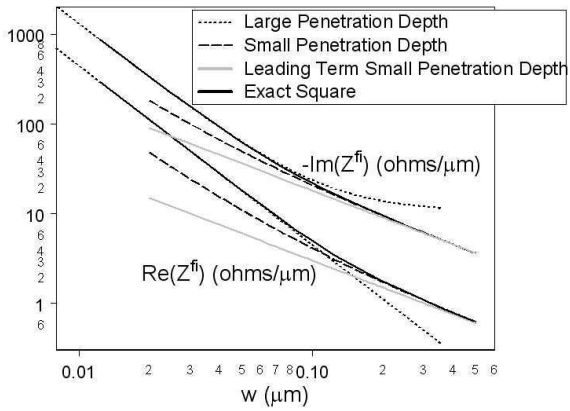

Figure 5. A comparison of the infrared impedance per unit length of a square conductor from the limiting formulas and an exact numerical calculation.

For infrared frequencies we can replace σ in (50) by $-i\omega\varepsilon$ and write

$$Z^{fi} \sim \frac{1}{-i\omega\varepsilon A} - i\omega L^{fi} \tag{55}$$

A comparison of the preceding high-frequency single term and three-term expansions (45) versus this low-frequency expansion, along with numerical values from an integral-equation solution [7], are shown in Figure 5 for a square conductor using the material properties of gold at a ten-micron wavelength (presented in Section 2.3.1). One can see that the concatenation of the two expansions together give a reasonable uniform description of the internal impedance per unit length.

2.3.4. High-frequency Strip

Another important case is the thin strip, where one dimension is small compared to the penetration depth. We assume now that we have a thin strip with width $w = 2b$ with a thin-sheet surface impedance of

$$Z_s = 1/(\sigma\Delta/2) \tag{56}$$

where the conductivity is σ, the sheet thickness is Δ, and the boundary condition on the surface of the strip is

$$E_z(x,0) = \frac{1}{2} Z_s \left[H_x(x,-0) - H_x(x,+0)\right] \tag{57}$$

We assume here that the skin depth satisfies $\delta \gg \Delta$. In this limit the current density is uniform in the strip thickness but not necessarily uniform along the strip width (a thin-sheet impedance electrical length scale of $1/\ell_0 = Z_s/(\omega\mu_0)$ replaces the skin depth in this limit). In this case the equivalent radius is

$$a = w/4 = b/2 \tag{58}$$

The iterative solution for the internal-impedance per unit length in a thin strip conductor is [10]

$$\begin{aligned} Z^{fi}/R_0 \;=\; & \frac{2}{\pi^2}\left[\ln(8\ell_0 b) + 1 + \gamma' - i\frac{\pi}{2}\right] \\ & + \frac{2}{\pi^2}\left(\frac{1}{2\ell_0 b}\right)\left[\left(1 - \frac{1}{4e^{1+\gamma'}}\right)\left\{\ln(8\ell_0 b) + \gamma'\right\}\right. \\ & \left. + \frac{i}{\pi}\left\{\gamma' + \ln(8\ell_0 b)\right\}\left\{\ln(8\ell_0 b) + 1/2 + \gamma'\right\}\right] - i\pi/4 \end{aligned} \tag{59}$$

for $b\ell_0 \to \infty$ where Euler's constant is $\gamma' = 0.5772156649$. Here

$$\ell_0 \;=\; \omega\mu_0/Z_s \tag{60}$$

$$R_0 \;=\; 1/(\sigma\Delta w) \tag{61}$$

Again for the infrared we can replace σ by $-i\omega\varepsilon$, and in this case with $\gamma\Delta/2 \ll 1$ but $\gamma^2(\Delta/2)w/2 \gg 1$, where

$$\gamma^2 = \omega^2\mu_0\varepsilon \tag{62}$$

we find

$$\begin{aligned}
&(-i\omega\varepsilon\Delta w)Z^{fi} \\
&= \frac{2}{\pi^2}\left[\ln\left(-i2\gamma^2\Delta w\right) + 1 + \gamma' - i\frac{\pi}{2}\right] \\
&\quad + \frac{2}{\pi^2}\left(\frac{1}{-i\gamma^2\Delta w/2}\right)\left[\left(1 - \frac{1}{4e^{1+\gamma'}}\right)\left\{\ln\left(-i2\gamma^2\Delta w\right) + \gamma'\right\}\right. \\
&\quad \left. + \frac{i}{\pi}\left\{\gamma' + \ln\left(-i2\gamma^2\Delta w\right)\right\}\left\{\ln\left(-i2\gamma^2\Delta w\right) + 1/2 + \gamma'\right\} - i\frac{\pi}{4}\right]
\end{aligned} \tag{63}$$

2.3.5. Low-frequency Strip

The low-frequency approximation can be found from the preceding rectangular result (49) as

$$Z^{fi} \sim R_0 - i\frac{\omega\mu_0}{2\pi}\left[\frac{3}{2} - 2\ln(2)\right] \tag{64}$$

for $(\omega\mu_0\sigma\Delta/2)w/2 = b\ell_0 = \omega\mu_0/(4R_0) \to 0$ where ℓ_0 and R_0 have been defined in the preceding section.

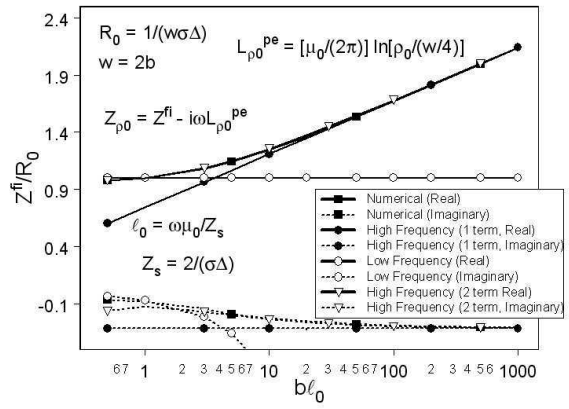

Figure 6. A comparison of the microwave impedance per unit length of an electrically thin strip from the limiting case formulas versus a numerical calculation.

Figure 6 shows a comparison of the thin-strip high frequency formulas with one and two terms (59), the low-frequency formulas (64), and a numerical integral equation solution [10] for the thin strip in the microwave range (the results are normalized so they apply to any high-conductivity metallic strip that is electrically thin).

Again for the infrared we can replace σ by $-i\omega\varepsilon$ to obtain

$$Z^{fi} \sim \frac{1}{-i\omega\varepsilon\Delta w} - i\frac{\omega\mu_0}{2\pi}\left[\frac{3}{2} - 2\ln(2)\right] \tag{65}$$

where $\gamma^2(\Delta/2)w/2 \to 0$ with (62).

2.4. Modeling of Wires

The preceding results give the equivalent radii (required to match the external inductance and capacitance per unit length) and the internal impedance per unit length. To model the response of a metallic trace we use these quantities in the thin-wire algorithm of the integral equation code EIGER [11, 12] with the electric equivalent radius a_e. The code solves the equation (which is the dual of the slot equation [13] and other wire antenna models [14])

$$E_s(a_e, s) + \Delta Z_C \frac{d^2 I}{ds^2} - \Delta Z_L I = -E_s^{inc}(s) \tag{66}$$

To correct the inductance per unit length and add in the internal impedance per unit length we set

$$\Delta Z_L = Z^{fi} - i\omega\frac{\mu_0}{2\pi}\ln(a_e/a) \tag{67}$$

$$\Delta Z_C = 0 \tag{68}$$

In this manner the current I is obtained as a function of the position along the trace s.

3. GAPS AND LUMPED LOADS

Another feature often found in metallic resonators are gaps or loads, which are usually used to downshift the resonant frequency of the unit cell. Figure 7(a) shows a gap in a trace positioned on a substrate. It is advantageous to capture the gap or load with the minimum computational resources being expended in this local region.

The idea is to define a load (G_0 might be present if lossy material exists in the gap) as shown in Figure 7(b) where

$$Y_0 = G_0 - i\omega C_0 \tag{69}$$

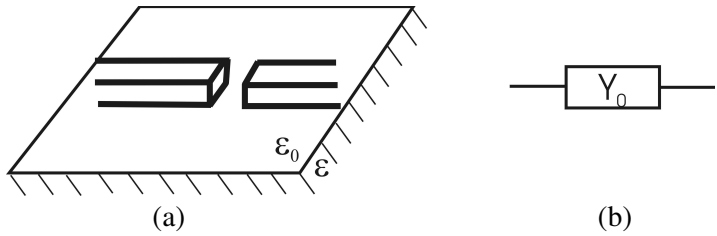

Figure 7. (a) A gap in a trace such as found in a split ring resonator. (b) Load Y_0 used in the thin-wire model must capture actual gap properties (including fringing) and remove extraneous additions due to the segments or facets.

and takes into account the properties of the gap (versus the thin wire, discussed in the next section) minus any extra effects caused by the segmentation or faceting of the thin-wire model used to simulate the resulting wire structure (or other differences between the classical thin wire and how it is represented in the simulation). The approach is similar to that used for the feed region in antenna theory [15].

3.1. Local Nature of Gap Capacitance

This section discusses the nature of the gap capacitance and develops the framework on how to construct a fit function to it. There are three things to consider: 1) how the thin wire should be defined, 2) how the thin-wire approximation differs from the actual gap geometry, and 3) how the discretized wire in the simulation differs from the continuous thin wire. Although these items could be lumped together to evaluate how the discretized thin wire structure differs from the actual trace, there is more insight provided by considering them separately; in addition, 2) ties in with older literature on approximations to wire antennas derived by means of Hallén iteration (where series expansions of capacitance in the inverse fatness parameter of the wire are generated), while 3) could be modified for different interpolation and quadrature schemes for other numerical methods.

If we have an infinite cylinder with a delta-gap voltage source V at its center, the charge per unit length on its exterior surface is

$$q_C(z) = 2a\varepsilon_0 V \int_0^\infty \frac{K_1(\zeta a)}{K_0(\zeta a)} \sin(\zeta z) d\zeta \tag{70}$$

If we take the limit of small a in the modified Bessel functions we arrive

at the thin-wire result [16–18] with

$$q_H(z) = -2\varepsilon_0 V \int_C \frac{\sin(\zeta z)}{\ln(\zeta/\zeta_p)} \frac{d\zeta}{\zeta}$$
$$= -2\varepsilon_0 V \left[P \int_0^\infty \frac{\sin(\zeta z)}{\ln(\zeta/\zeta_p)} \frac{d\zeta}{\zeta} - \pi \cos(\zeta_p z) \mathrm{sgn}(z) \right] \quad (71)$$

where P stands for principal-value integral and a pole has been introduced by the approximation at

$$\zeta_p = 2/\left(ae^{\gamma'}\right) \quad (72)$$

For $z > 0$ the contour C is chosen to be indented slightly above the pole for the $e^{i\zeta z}$ component and slightly below for the $e^{-i\zeta z}$ component, giving the final principal value result on the right; with this definition the charge per unit length vanishes at $z \to \infty$. If we use the averaging method to evaluate the integral [19] and use

$$\langle \ln(\zeta/\zeta_p) \rangle \int_0^\infty \sin(\zeta z) \frac{d\zeta}{\zeta} = \int_0^\infty \ln(\zeta/\zeta_p) \sin(\zeta z) \frac{d\zeta}{\zeta}$$
$$= -\frac{\pi}{2} \left[\ln\left(\zeta_p |z|\right) + \gamma' \right] \mathrm{sgn}(z) \quad (73)$$

we find the approximation to (71) as

$$q_H(z) \approx -2\varepsilon_0 V \int_0^\infty \frac{\sin(\zeta z)}{\langle \ln(\zeta/\zeta_p) \rangle} \frac{d\zeta}{\zeta} = \frac{\pi \varepsilon_0 V}{\ln\left(2|z|/a\right)} \mathrm{sgn}(z) \quad (74)$$

where the identity [20]

$$\int_0^\infty \zeta^{\beta-1} \sin(\zeta z) d\zeta = \frac{\pi \sec(\beta\pi/2)}{2|z|^\beta \Gamma(1-\beta)} \mathrm{sgn}(z) \quad (75)$$

has been used. This is quite accurate for $z/a > 4$ as shown in Figure 8.

By subtracting this charge density from that of the actual geometry q we can define a difference charge and capacitance that is localized near the gap. That is,

$$\Delta C = \Delta Q/V = \frac{1}{V} \int_0^\infty (q - q_H) dz \quad (76)$$

where consequently this allows the actual gap geometry to be treated on a structure with simple straight arms rather than the more complicated loop resonator.

A simple illustration is provided by a hollow tubular cylinder having a narrow gap $g \ll a$. In this case we begin with the charge per unit length given by

$$q_T(z) = 2a\varepsilon_0 V \int_0^\infty \left[\frac{K_1(\zeta a)}{K_0(\zeta a)} + \frac{I_1(\zeta a)}{I_0(\zeta a)} \right] \sin(\zeta z) d\zeta \quad (77)$$

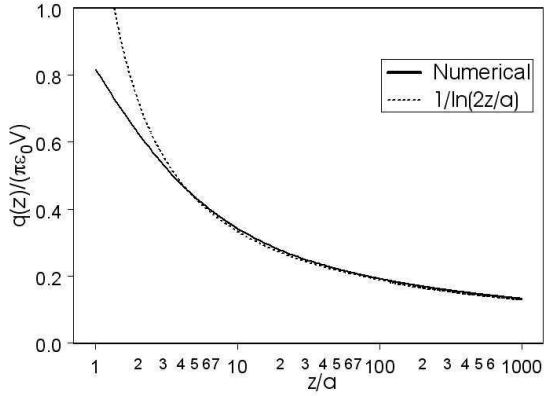

Figure 8. Exact evaluation of Hallen thin-wire charge distribution versus a simple averaging evaluation.

for a tube with a delta gap. This tube charge per unit length on the cylinder with the delta gap approximates the actual charge density $q(z)$ down to some distance $z = g_0$, where $a \gg g_0 \gg g/2$, and the difference charge is then calculated as

$$\begin{aligned}\Delta Q_T &= \int_{g_0}^{\infty} (q_T - q_H) dz \\ &= 2\varepsilon_0 V \int_0^{\infty} \left[\frac{1}{K_0(\zeta a) I_0(\zeta a)} + \frac{1}{\ln(\zeta/\zeta_p)} - \frac{2a^2\zeta^2}{\zeta a + 1} \right] \cos(\zeta g_0) \frac{d\zeta}{\zeta^2} \\ &\quad + a \left\{ \cos(g_0/a) \mathrm{Ci}(g_0/a) + \sin(g_0/a) \mathrm{si}(g_0/a) \right\} \end{aligned} \tag{78}$$

Here the Wronskian has been used and the final term in the integrand has been subtracted and added (in terms of the sine and cosine integrals) to improve the convergence at $\zeta \to \infty$,

$$\mathrm{si}(x) = -\int_x^{\infty} \frac{\sin u}{u} du \tag{79}$$

$$\mathrm{Ci}(x) = -\int_x^{\infty} \frac{\cos u}{u} du \tag{80}$$

[6]. Because we are interested in the result for $g_0 \ll a$, and with the improved convergence we can set the cosine to unity and expand the sine and cosine integrals to obtain

$$\Delta Q_T / (2a\varepsilon_0 V) = \frac{1}{2\varepsilon_0 a V} \int_{g_0}^{\infty} (q_T - q_H) dz$$

$$= \int_0^\infty \left[\frac{1}{K_0(u)I_0(u)} + \frac{1}{\ln(u/2)+\gamma'} - \frac{2u^2}{u+1}\right]\frac{du}{u^2} - 2\left\{\ln(g_0/a)+\gamma'\right\} \quad (81)$$

Evaluation of the integral yields

$$\Delta C_T/(2a\varepsilon_0) = \Delta Q_T/(2a\varepsilon_0 V) \approx 2\ln(a/g_0) - 2\gamma' - 0.2225 \quad (82)$$

Now near the gap we can use the two-dimensional conformal mapping result for the charge density about a slot of gap g to write the normal field as

$$E_r(a \pm 0, z) = \pm\frac{V/\pi}{\sqrt{z^2-(g/2)^2}} \quad (83)$$

where $a \gg z > g/2$. Integration of the charge gives

$$C_{g_0}/(2a\varepsilon_0) = Q_{g_0}/(2a\varepsilon_0 V) = (2\pi/V)\int_{g/2}^{g_0} E_r(a+0,z)dz = 2\text{arccosh}(2g_0/g) \sim 2\ln(4g_0/g) \quad (84)$$

Thus adding this to the tube gives the lumped correction to the thin wire for the capacitance of a thin-walled tube (including both interior and exterior regions)

$$\Delta C_{\text{tube}}/(2a\varepsilon_0) = \Delta C_T/(2a\varepsilon_0) + C_{g_0}/(2a\varepsilon_0) \approx 2\left\{\ln(4a/g) - \gamma' - 1/9\right\} \quad (85)$$

This form will be referred to in the segment or facet correction below.

A second illustration is the cylinder with flat end caps. In this case we use the preceding exterior representation to find

$$\Delta Q_C/(2a\varepsilon_0 V) = \frac{1}{2\varepsilon_0 aV}\int_{g_0}^\infty (q_C - q_H)dz = \int_0^\infty \left[u\frac{K_1(u)}{K_0(u)} + \frac{1}{\ln(u/2)+\gamma'} - \frac{u^2}{u+1}\right]\frac{du}{u^2} - \left\{\ln(g_0/a)+\gamma'\right\} \quad (86)$$

Numerical evaluation gives

$$\Delta C_C/(2a\varepsilon_0) = \Delta Q_C/(2a\varepsilon_0 V) \approx \ln(a/g_0) - \gamma' - 0.133150 \quad (87)$$

In this case to add in the right-angle edge and the flat end caps in the gap, we replace $g/4$ in C_{g_0} by $g/(\pi e/2) \approx g/4.269867$ [21] and add in the parallel-plate capacitance to obtain the correction to the thin wire for a cylinder with flat end caps (in this case only the exterior region is present except in the gap). This gives

$$\Delta C_{cyl}/(2a\varepsilon_0) = \left(\Delta C_C + C_{g_0} + C_{pp}\right)/(2a\varepsilon_0) \approx \ln\left(\frac{\pi a}{2g}\right) + 1 - \gamma' - 2/15 + \frac{\pi a}{2g} \quad (88)$$

This result forms the basis for the capacitive correction for metallic traces by use of the equivalent radius of the trace. If there is a substrate then $2\varepsilon_0 \to (\varepsilon + \varepsilon_0)$ and $a \to a_e$. By representing the actual trace geometry near the gap in a three-dimensional static solution (we used a static version of EIGER (EIGER_S) for this purpose [11]) we can find the actual local charge per unit length q and then determine the smaller correction f_{cyl} to further improve the accuracy of this load. With this correction, we have

$$\Delta C = \frac{1}{V}\int_0^\infty (q - q_H)dz = \Delta C_{cyl} + (2a\varepsilon_0)f_{cyl}(g/a) \tag{89}$$

3.2. Cylinder Gap Capacitance

The case where the cross section is a circular tube of radius a half embedded in a substrate (a is the equivalent radius since it is half embedded, as opposed to resting on a substrate as in (13)) has the gap capacitance (here we assume the substrate fills the bottom half of the gap) of

$$\begin{aligned}\Delta C \;=\; & (\varepsilon + \varepsilon_0)a\left[\ln(\pi a/(2g)) + 1 - \gamma' - 2/15\right] \\ & +(\varepsilon + \varepsilon_0)af_{cyl}(g/a) + C_{pp}\end{aligned} \tag{90}$$

where [3]

$$f_{cyl}(x) = 0.02 - 0.12x \tag{91}$$

A comparison of this simple fit (91) with numerical values from the three-dimensional static simulation is shown in Figure 9. The parallel plate term for the gap interior in this case is

$$C_{pp} = (\varepsilon + \varepsilon_0)\pi a^2/(2g) \tag{92}$$

3.3. Strip Gap Capacitance

By analogy with the tube, in the case of a thin strip $t/w \to 0$ by noting that $a_0 = w/4$ and

$$\begin{aligned}C_{g_0} &\approx w\frac{\varepsilon + \varepsilon_0}{V}\int_{g/2}^{g_0} E_r(a + 0, z)dz = \frac{w}{\pi}(\varepsilon + \varepsilon_0)\text{arccosh}(2g_0/g) \\ &\sim \frac{w}{\pi}(\varepsilon + \varepsilon_0)\ln(4g_0/g) = \frac{P}{2\pi}(\varepsilon + \varepsilon_0)\ln(4g/g_0)\end{aligned} \tag{93}$$

we take

$$\begin{aligned}\Delta C \approx\; & (\varepsilon + \varepsilon_0)\frac{P}{2\pi}\left[\ln(4a_0/g) - \gamma' - 2/15\right] \\ & +(\varepsilon + \varepsilon_0)a_0 f_{\text{strip}}(g/a_0)\end{aligned} \tag{94}$$

$$f_{\text{strip}}(1/4) \approx +0.144 \tag{95}$$

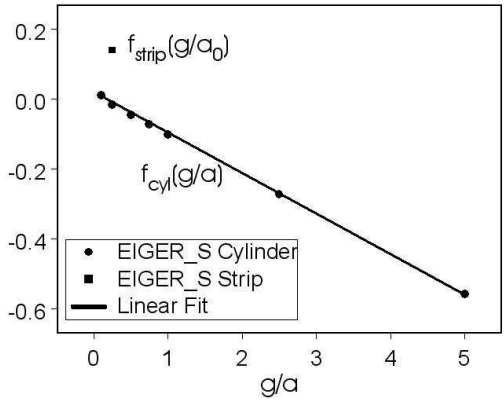

Figure 9. Comparison of the simple fit (91) as a function of g/a and the numerical values obtained from a three-dimensional static simulation using EIGER_S. Also shown is a result for the thin strip.

where $P = 2w$ is the strip cross section perimeter. (Note that there is actually no rigorous extrapolation for the first term since $P/(2\pi) = w/\pi \neq a_0 = w/4$ and we expect the correction f_{strip} to make up for the error). Here we have used the exterior only result because the interior of the strip does not exist (we do not use the right angle equivalent radius but the thin limit).

3.4. Rectangle Gap Capacitance

By analogy with the cylinder we take the rectangle cross section to have the gap capacitance correction

$$\Delta C \approx (\varepsilon + \varepsilon_0)\frac{P}{2\pi}\left[\ln(\pi a_e/(2g)) + 1 - \gamma' - 2/15\right] + (\varepsilon + \varepsilon_0)a_e f_{rect}(t/w, g/w, \varepsilon/\varepsilon_0) + C_{pp} \quad (96)$$

$$C_{pp} = \varepsilon_0 wt/g \quad (97)$$

where $P = 2(w + t)$ is the rectangular cross section perimeter. (Again, there is actually no rigorous extrapolation for the first term since $P/(2\pi) \neq a_e$ and we expect the correction f_{rect} to make up for the error.) The value of the correction term f_{rect} for design B (described in Section 2.2), a near square with equal gap to thickness, has been determined from three-dimensional static simulations (EIGER_S) of a long trace with a gap on a substrate to be

$$f_{rect}(\text{design B}) = f_{rect}(5/6, 5/6, 10.8924) \approx -0.375 \quad (98)$$

In the case when the substrate is not present this correction was numerically found to be

$$f_{rect}(5/6, 5/6, 1) \approx -0.387 \tag{99}$$

3.5. Segment or Facet Corrections

The algorithm used in EIGER to treat the thin wire uses an elliptic kernel to treat the wire and thus includes both the interior and exterior regions of the tube. Hence, because of the finite quadrature scheme used for the moments, there is a finite capacitance due to the local region near the gap of a wire structure (where a lumped load is placed to account for the proper capacitance). This capacitance depends on the segment or facet length and was empirically determined to be

$$\Delta C_s = \int_0^\infty (q_E - q_H) dz \approx 2a_e(\varepsilon + \varepsilon_0) \left[\ln(4a_e/g_s) - \gamma' - 1/9\right] \tag{100}$$

where

$$g_s \approx s_0/3.4 \tag{101}$$

[3] and s_0 is the segment or facet length at the gap.

3.6. Load Capacitance

Since we have focused on lossless gaps $G_0 = 0$ and

$$C_0 = \Delta C - \Delta C_s \tag{102}$$

4. COMPARISONS AND EXAMPLES

The subcell-wire algorithms will be illustrated on two examples: 1) the split-ring magnetic resonator shown in Figures 10(a) and 10(c) with the equivalent wire model shown in Figure 10(b); and 2) the Z electric dipole particle shown in Figure 11(b). This particular Z particle does not have a gap, whereas the SRR does; although loads could be incorporated at the ends of the Z particle arms for extra accuracy, we will not consider them here.

4.1. SRR & Z Dipole Metafilm

For an SRR design that we call "design B", the dimensions labeled in Figure 11(a) are $\ell \approx 0.54\,\mu$m, $w \approx 0.12\,\mu$m, $t \approx 0.1\,\mu$m, $g \approx 0.1\,\mu$m, and the metafilm lattice period is equal to $d \approx 1.34\,\mu$m. For design B, the SRR is made of Gold (Au) and is placed on a Gallium Arsenide (GaAs) substrate with dielectric constant $\varepsilon/\varepsilon_0 \approx 10.8924$.

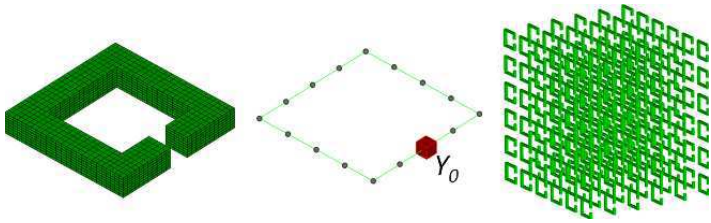

Figure 10. (a) SRR with explicit surface mesh. (b) Thin wire SRR subcell model with lumped load accounting for SRR gap. (c) Array of SRRs cells forming a metamaterial.

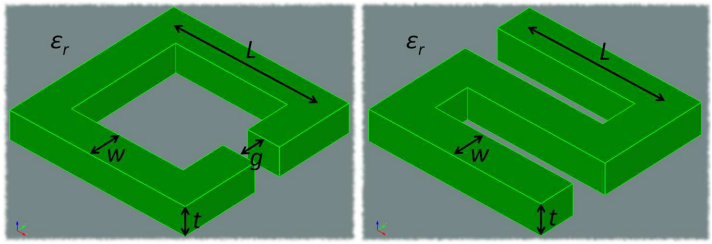

Figure 11. An (a) SRR and (b) Z dipole on a dielectric substrate, shown with the metallic-trace dimensions. The length dimension is the same in the orthogonal directions.

Based on the analysis presented in the previous sections, the resulting trace parameters for this near-square trace case are

$$a \approx 1.18(w+t)/4 \approx 0.065\,\mu\text{m} \tag{103}$$

$$a_e \approx 0.036\,\mu\text{m} \tag{104}$$

and substituting $2b \to (w+t)/2$ in (45)

$$Z^{fi} \approx 3.62 - i18.55\,\text{Ohms}/\mu\text{m} \tag{105}$$

For the calculation of the impedance per unit length, the Au permittivity at 10 microns has been used (30). From Section 3, the load parameters are $\Delta C \approx -2.405\,\text{aF}$ and $\Delta C_s \approx 9.875\,\text{aF}$ and thus

$$C_0 \approx -12.28\,\text{aF} \tag{106}$$

Figure 12(a) shows a comparison of the full-mesh simulation with the subcell simulation for the design B SRR (on a GaAs substrate) when excited by a normally-incident plane wave (the incident electric field

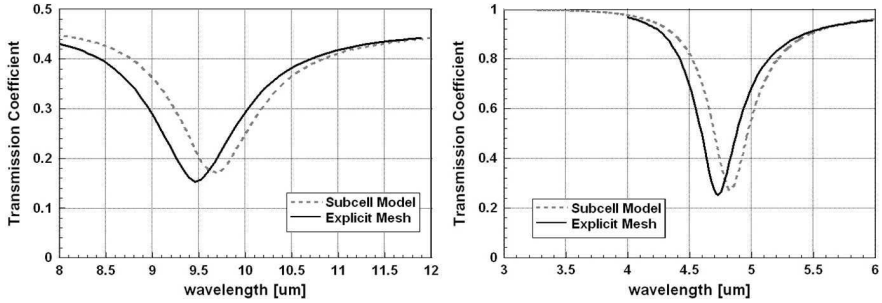

Figure 12. Comparison of the transmission coefficient from the subcell and full mesh simulations for (a) a planar layer of SRRs on a GaAs substrate and (b) a planar screen of periodic SRRs in air. Both arrays are excited by the electric field of a normally incident plane wave.

drives the SRR in this configuration). For both of these simulations gold dispersion properties were used over the 8–12 μm bandwidth. The subcell model consisted of 32 segments (which was sufficient for convergence) and unknown currents around the loop and the full mesh in EIGER had approximately 30,000 unknowns (the full-mesh with this resolution demonstrated convergence influenced by the metallic penetration of the fields). Both simulations implemented a periodic metafilm through the moment method Green's function, so the meshes specified here were for a single particle. The run times per frequency point for the full mesh were about 3.5 hours on 64 processors versus 8 seconds on 1 processor for the subcell (this several order of magnitude improvement in run times is typical of the other comparisons given in this paper). The agreement is quite good and is in fact better than we found with many commercial software packages using the available unknowns (memory) on a workstation.

The design B SRR was considered without the substrate (with the same dimensions as described above) and a comparison of the explicit mesh to subcell results (in air) are shown in Figure 12(b). Again the agreement is reasonably good. It is interesting that if we consider the fact that the current centroids of two neighboring oppositely directed currents (at least for cylinders of radius a and infinite length) are displaced from center-to-center spacing ℓ to spacing $\sqrt{\ell^2 - 4a^2}$, then the resonant position in the subcell model is changed from 4.83 μm to 4.71 μm, versus the full mesh position of 4.73 μm. This slight

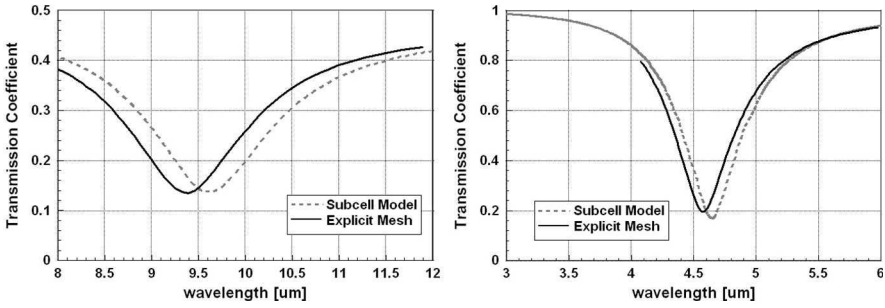

Figure 13. Comparison of the transmission coefficient from the subcell and full mesh simulations for (a) a planar layer of Z-dipoles on a GaAs substrate and (b) a planar screen of periodic Z-dipoles in air. Both arrays are excited by the electric field of a normally incident plane wave.

overcompensation of resonant position is thought to be caused by the fact the side containing the gap has a smaller current than the opposing side, and thus the preceding shift in position is too great for these two sides (in fact if the shift in position is left out for these two sides we find a resonant wavelength in the resulting rectangular subcell of 4.76 μm). These approximate comparisons, which bracket the full mesh resonant position, indicate that shifts in current centroid positions are likely responsible for the shifts observed in the subcell versus full mesh comparisons. A general method for improving the wire subcell model approximation is to introduce line multipoles (rather than the filament alone) into the subcell model.

Figure 13(a) shows the comparison of the transmission coefficient for a periodic array of Z particles on a GaAs substrate for both the full mesh and subcell simulations (consisting of 21 segments). The dimensions of the Z particle are $\ell \approx 0.57\,\mu\text{m}$, $w \approx 0.12\,\mu\text{m}$, $t \approx 0.1\,\mu\text{m}$ and the metafilm lattice period is equal to $d \approx 1.34\,\mu\text{m}$. Figure 13(b) shows the comparison of the transmission coefficient for a periodic array of Z particles in air with both the full mesh and subcell simulations. Again the agreement in this figure is good.

4.1.1. Insulation Layer

Note that if there is a very thin insulation layer with permittivity ε_1 and thickness $h_1 \ll w$ below the rectangular trace as shown in the inset of Figure 14(b) we can redefine the capacitance per unit length

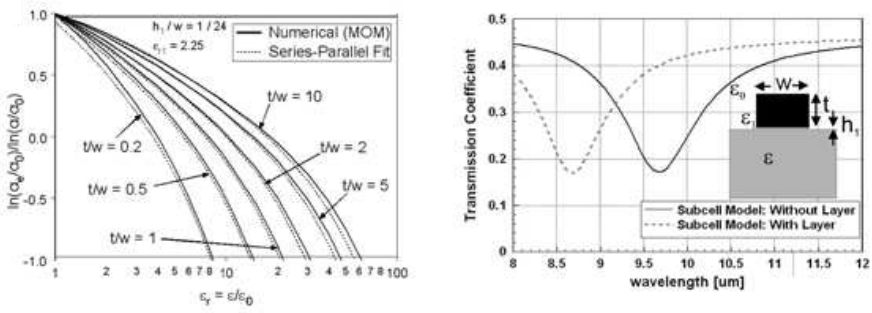

(a) (b)

Figure 14. (a) Electric equivalent radius for a metallic trace on thin insulation layer of thickness 0.005 nm and relative permittivity 2.25. (b) Subcell model results with and without the insulation layer for a trace of $t = 0.1\,\mu\text{m}$ and $w = 0.12\,\mu\text{m}$.

as

$$C_{a_1} = \frac{2\pi\varepsilon_0}{\ln(a_1/a)} - \frac{\pi\varepsilon_0}{\ln(a_1/a_0)} + C_{h1} \tag{107}$$

$$1/C_{h1} = \frac{\ln(a_1/a_0)}{\pi\varepsilon} + \frac{h_1}{w\varepsilon_1} \tag{108}$$

to capture this effect. For this case, the equivalent electric radius is then changed to

$$\frac{\ln(a_e/a_0)}{\ln(a_1/a_0)} = 1 - \frac{(\varepsilon/\varepsilon_0+1)}{2\frac{\ln(a_1/a_0)}{\ln(a_1/a)} - 1 + \ln(a_1/a_0)/\left[\frac{\ln(a_1/a_0)}{(\varepsilon/\varepsilon_0)} + \frac{\pi(h_1/w)}{(\varepsilon_1/\varepsilon_0)}\right]} \tag{109}$$

As an example we can address a thin oxide layer under a metallic trace with $h_1 \approx 5\,\text{nm}$ and $\varepsilon_1 \approx 2.25\varepsilon_0$. This results in an effective radius of $a_e \approx 0.023\,\mu\text{m}$ (the numerical calculation gives 0.0233, (109) gives 0.0227) which is less than $a_0 \approx 0.03\,\mu\text{m}$ (12) (as a consequence of the oxide). Figure 14(a) shows a comparison of numerical values for this case versus the preceding modified fit (the numerical values were generated by displacing the rectangular conductor upward by distance $h_1/(\varepsilon_1/\varepsilon_0)$ with air present to obtain the same parallel plate capacitance in the extremely thin layer).

The gap capacitance also changes in this case. The preceding rectangular formula for ΔC is used in this case but f_{rect} is replaced by

$$\begin{aligned} f_{rect}\,(\text{design B oxide}) &= f_{rect}(t/w, g/w, \varepsilon/\varepsilon_0, h_1/w, \varepsilon_1/\varepsilon_0) \\ &= f_{rect}(5/6, 5/6, 10.8924, 1/24, 2.25) \\ &\approx +0.150 \end{aligned} \tag{110}$$

and thus inserting the new a_e into the segment correction ΔC_s we finally arrive at

$$C_0 = \Delta C - \Delta C_s \approx -8.06\,\text{aF} \tag{111}$$

Figure 14(b) shows the resonant wavelength shift resulting from the extremely thin oxide layer. Experiments and simulations illustrating this effect have been published previously [22].

4.2. SRR & Z Dipole Media

This same SRR was now scaled in dimension to $\ell \approx 1.14\,\mu\text{m}$, $w \approx 0.25\,\mu\text{m}$, $t \approx 0.21\,\mu\text{m}$, $g \approx 0.21\,\mu\text{m}$, $d \approx 2.82\,\mu\text{m}$, to position the resonance in air near the same ten-micron wavelength. The SRR was also rotated to be excited by the incident magnetic field (incident magnetic field through the loop, with the incident electric field along the uncut arms) and a layer with five SRRs in the propagation direction and infinite periodicity in the lateral directions was created to form a magnetic media. A comparison of the transmission coefficient for this layer with the full mesh and the subcell model is shown in Figure 15(a). Except for a small frequency shift the agreement is reasonable.

In order to form an electric media, Z dipoles as shown in 11(b) were used to form a periodic layer with five dipoles in the direction of propagation. The dimensions (Figure 11(b)) used for the Z dipole were $\ell \approx 1.34\,\mu\text{m}$, $w \approx 0.25\,\mu\text{m}$, $t \approx 0.21\,\mu\text{m}$, and $d \approx 2.82\,\mu\text{m}$. Straight-loaded dipoles, as shown in Figure 1(b), could also be used where an inductive load at microwave frequencies or a polaritonic-material load (with intrinsic negative permittivity) in the infrared would generate a

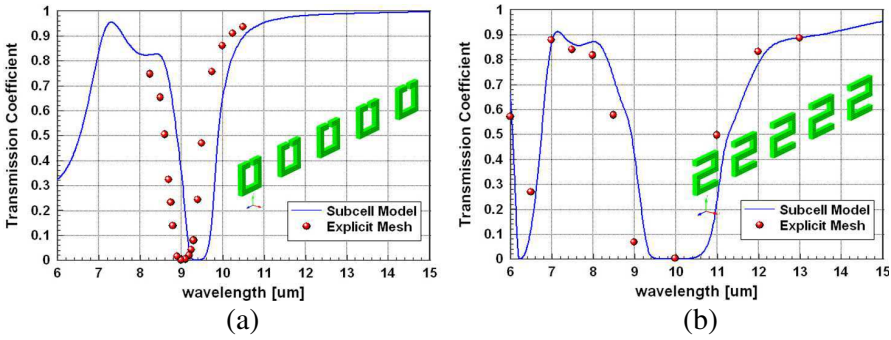

Figure 15. Comparison of subcell and full mesh simulations for a 5-layer thick periodic layer (in air) comprised of (a) SRRs excited by the incident magnetic field and (b) Z-dipoles excited by the incident electric field.

downshift in the resonant frequency. A comparison of the simulated transmission coefficients for a five-deep Z-dipole layer based on a full-surface mesh and a subcell model is shown in Figure 15(b). With the exception of a small frequency shift, the agreement is again reasonable. In both simulations of Figure 15, the relatively sparse frequency sampling of the full-mesh simulations is indicative of the significant computational intensity and run times that are associated with high-resolution surface meshes in the IR frequency regime.

5. CONCLUSIONS

This paper introduces a computational approach that simplifies the simulations of metallic-metamaterial resonators in the microwave and infrared frequency regimes. The approach is to use thin-wire models for the metallic traces where we embed known characteristics of the impedance per unit length for the narrow metallic traces. Resonators resting on dielectric substrates are included by introduction of different equivalent radii for the magnetic and electric problems. In addition the local gap features are modeled by lumped loads that produce the proper capacitance while removing extraneous segment or facet contributions. The results show good agreement with full-mesh simulations, but are able to achieve one thousand to one reductions in computational complexity and run times.

ACKNOWLEDGMENT

Sandia National Laboratories is a multi-program laboratory managed and operated by Sandia Corporation, a wholly owned subsidiary of Lockheed Martin Corporation, for the U.S. Department of Energy's National Nuclear Security Administration under contract DE-AC04-94AL85000.

REFERENCES

1. Tretyakov, S., *Analytical Modeling in Applied Electromagnetics*, Artech House, 2003.
2. Grzegorczyk, T. M., C. D. Moss, J. Lu, X. Chen, J. Pacheco, Jr., and J. A. Kong, "Properties of left-handed metamaterials: Transmission, backward phase, negative refraction, and focusing," *IEEE Trans. on Microwave Theory and Tech.*, Vol. 53, No. 9, Sep. 2005.

3. Johnson, W. A., L. K. Warne, L. I. Basilio, W. L. Langston, and M. B. Sinclair, "Subcell models with applications to split-ring resonators," *IEEE APS-Symp.*, Spokane, WA, Jun. 2011.
4. Marcuvitz, N., *Waveguide Handbook*, 263–264, Peter Peregrinus, Ltd., London, 1986.
5. Warne, L. K., "Eddy current power dissipation at sharp corners: Rectangular conductor examples," *Electromagnetics*, Vol. 15, 273–290, 1995.
6. Abramowitz, M. and I. A. Stegun (eds.), *Handbook of Mathematical Functions*, 231–233, 374–379, 589–592, Dover, New York, 1972.
7. Warne, L. K., "Eddy current power dissipation at sharp corners," *IEEE Trans. on Microwave Theory and Tech.*, Vol. 42, No. 2, Feb. 1994.
8. Kaye, G. W. C. and T. H. Laby, *Tables of Physical and Chemical Constants*, 117, Longman Scientific & Technical, John Wiley & Sons, Inc., New York, 1989.
9. Cockcroft, J. D., "Skin effect in rectangular conductors at high frequencies," *Proceedings Royal Society*, Vol. 122, 533–542, 1929.
10. Warne, L. K. and W. A. Johnson, "Asymptotic expansion of the impedance per unit length of thin strip conductors," Sandia National Laboratories, 2005.
11. Johnson, W. A., L. I. Basilio, J. D. Kotulski, R. E. Jorgenson, L. K. Warne, R. Coats, D. Wilton, N. Champagne, F. Capolino, J. Grant, and M. Khayat, "EIGER: An open-source frequency domain electromagnetics code," *IEEE APS-Symp.*, Honolulu, Hawaii, 2007.
12. Khayat, M. A. and D. R. Wilton, "Numerical evaluation of singular and near-singular potentials integrals," *IEEE Trans. on Antennas and Propagation*, Vol. 53, No. 10, 3180–3190, Oct. 2005.
13. Warne, L. K. and K. C. Chen, "Slot apertures having depth and losses described by local transmission line theory," *IEEE Trans. on Electromagnetic Compatibility*, Vol. 32, No. 3, 185–196, Aug. 1990.
14. Chen, K. C. and L. K. Warne, "A uniformly valid loaded antenna theory," *IEEE Trans. on Antennas and Propagation*, Vol. 40, No. 11, 1313–1323, Nov. 1992.
15. Schelkunoff, S. A., *Antenna Theory and Practice*, 302–322, 361–388, 584–585, John Wiley & Sons, Inc., New York, 1952.
16. Hallén, E., *Electromagnetic Theory*, Section 35.3, 61–64, Chapman and Hall, London, 1962.

17. Warne, L. K. and K. C. Chen, "Effective impedance of bolt loads on narrow slot apertures having depth," *Electromagnetic Waves and Applications*, Vol. 6, No. 7, 891–910, 1992.
18. Warne, L. K., "Low frequency capacitance of a tubular dipole," Sandia National Laboratories Internal Report, to R. H. Bonn, Dec. 14, 1990.
19. Chen, K. C. and L. K. Warne, "Improved asymptotic expansions of time domain antenna current," *Radio Science*, Vol. 26, No. 3, 1205–1208, Sep.–Oct. 1991.
20. Gradshteyn, I. S. and I. M. Ryzhik (eds.), *Table of Integrals Series and Products*, 420, Academic Press, New York, 1965.
21. Warne, L. K. and K. C. Chen, "Equivalent antenna radius for narrow slot apertures having depth," *IEEE Trans. on Antennas and Propagation*, Vol. 37, No. 7, 824–834, 1989.
22. Shelton, D. J., D. W. Peters, M. B. Sinclair, I. Brenner, L. K. Warne, L. I. Basilio, K. R. Coffee, and G. D. Boreman, "Effect of thin silicon dioxide layers on resonant frequency in infrared metamaterials," *Optics Express*, Vol. 18, No. 2, Jan. 18, 2010.